Analysis of lateral mode behavior in broad-area InGaN quantum well lasers

W.W.Chow

Sandia National Laboratories

Albuquerque, NM 87185-0601

H. Amano

Department of Electrical and Electronic Engineering

Meijo University

1-501 Shiogamaguchi

Tempaku-ku, Nagoya 468, Japan

(May 23, 2000)

Abstract

A wave-optical model that is coupled to a microscopic gain theory is used to investigate lateral mode behavior in group-III nitride quantum well lasers. Beam filamentation due to self-focusing in the gain medium is found to limit fundamental-mode output to narrow stripe lasers or to operation close to lasing threshold. Differences between nitride and conventional near-infrared semiconductor lasers arise because of band structure differences, in particular, the presence of a strong quantum-confined Stark effect in the former. Increasing mirror reflectivities in plane-plane resonators to reduce lasing threshold current tends to exacerbate the filamentation problem. On the other hand, a negative-branch unstable resonator is found to mitigate filament effects, enabling fundamental-mode operation far above threshold in broad-area lasers.

DISCLAIMER

I. Introduction

High-power, fundamental-mode operation is necessary in order to fully realize the advantages of the short wavelength in InGaN lasers, [1,2] in applications such as digital versatile disk and laser printers. Widening the gain region is the usual approach to scaling semiconductor lasers to high output powers. A limitation, if fundamental-mode operation is to be maintained, is the formation of filaments. [3] Filamentation is caused by self-focusing of the intracavity laser field in the semiconductor gain medium. After the onset of filamentation, the lateral dimension of the fundamental laser mode is constricted to the extent that in a broad-area laser, the overlap with a gain region is substantially reduced. The inversion that is not depleted by the fundamental mode then becomes available to the higher order lateral modes, thereby increasing the likelihood of multimode operation. Furthermore, filamentation gives rise to high intracavity intensities, which increase the possibility of material damage.

In this paper, we investigate filament formation in InGaN/GaN quantum well lasers. We use a wave-optical model to determine the intracavity laser field. The gain medium properties are obtained from a semiclassical laser theory that is based on the semiconductor Bloch equations, with collisions treated at the level of quantum kinetic equations in the Markovian limit. [4] The wave-optical laser model and the accompanying laser gain theory are described in Section II. Section III describes the properties of the gain medium affecting laser mode behavior. In particular, we discuss the carrier-induced refractive index, and its dependence on quantum well width. Also in this section, we introduce the concept of the antiguiding factor, which provides a measure of the strength of filamentation in a given quantum well structure. Section IV shows the effects of filamentation on lateral field distribution. We use two different InGaN/GaN quantum well gain regions to illustrate the effects of the quantum-confined Stark effect. [5,6] The effects of reducing internal optical losses is also discussed. In Section V, we study how laser modal properties are changed when resonator mirrors are coated to reduce lasing threshold. It is found that filamentation

effects amplify with increasing facet reflectivities, especially with the plane resonator mirrors presently used in nitride lasers. A result is the increased likelihood for multimode operation. We propose a solution to this problem in Section VI. By using unstable resonators, [7–10] single-mode operation may be maintained at high excitation in broad-area lasers operating with high reflectivity resonator mirrors. A parametric study shows that a negative-branch unstable resonator is best suited for nitride quantum well lasers, in terms of insensitivity to mirror curvatures, and enabling fundamental-mode operation far above lasing threshold in a broad-area stripe geometry. The results of this paper are summarized in Sec. VII

II. Theory

We adopt a coordinate system where y is the lateral (plane of quantum well) dimension, x is the transverse (perpendicular to quantum well plane) dimension, and z is along the resonator axis. The effective refractive index in the absence of an injection current, $n(\mathbf{r}) = n(x, y)$ is a weak function of y, especially for the gain-guided edge-emitting structures typically used for high power semiconductor lasers. This allows the two counter propagating intracavity laser fields to be written as

$$E_{\pm}(\mathbf{r}, t) = \sqrt{\frac{1}{2\epsilon_0 cn}} u(x, y) v_{\pm}(y, z) e^{i(\pm Kz - \omega t)} + c.c. \ , \tag{1}$$

where ε_0 and c are the permittivity and speed of light in vacuum, K and n are the laser wavevector and average refractive index in the host medium, and ω is the angular frequency. The total field is

$$E(\mathbf{r}, t) = E_{+}(\mathbf{r}, t) + E_{-}(\mathbf{r}, t) \ , \tag{2}$$

and we assume an electric field polarization in the plane of the quantum well. From Maxwell's equations, [11]

$$\pm \frac{\partial v_{\pm}}{\partial z} = \frac{i}{2K} \frac{\partial^2 v_{\pm}}{\partial y^2} + \Gamma \left[\frac{G(N)}{2} + i K_0 \delta n_g(N) \right] v_{\pm} - \alpha_{abs} v_{\pm} \ , \tag{3}$$

where $K_0 = K/n$, Γ is the confinement factor, α_{abs} accounts for the internal optical losses due to free-carrier absorption, scattering from the interfaces, and radiation through the cladding

layers, G is the local intensity gain and δn_g is the carrier-induced refractive index change. The transverse field distribution $u(x,y)$, which is a weak function of y, is determined by the epitaxial layers of the heterostructure.

The calculation of $G(N)$ and $\delta n_g(N)$ at each location in the gain region requires the simultaneous solution of the carrier density rate equation, and the microscopic equations describing the polarization due to electron-hole pairs. According to semiclassical laser theory and working in MKS units, [4]

$$G(N) = -\frac{\omega}{\varepsilon_0 ncE} \operatorname{Im} P(N) \tag{4}$$

$$K_0 \delta n_g(N) = -\frac{\omega}{2\varepsilon_0 ncE} \operatorname{Re} P(N) \ , \tag{5}$$

where E is the amplitude of the local laser field. The amplitude P of the induced polarization is

$$P(N) = \frac{2}{V} \sum_{\nu_e,\nu_h,\vec{k}} \left(\mu_{\vec{k}}^{\nu_e\nu_h}\right)^* p_{\vec{k}}^{\nu_e\nu_h}(N) e^{i\omega t} \ , \tag{6}$$

where V is the active region volume, $\vec{k}$ is the carrier momentum in the quantum-well plane, $\nu_e(\nu_h)$ identifies the conduction (valence) quantum-well subband, $\mu_{\vec{k}}^{\nu_e,\nu_h}$ is the optical dipole matrix element, and $p_{\vec{k}}^{\nu_e\nu_h}$ is the microscopic dipole due to an electron-hole pair. To calculate the microscopic dipole, we solve the semiconductor Bloch equations. Assuming quasiequilibrium electron and hole populations, $n_{\vec{k}}^{\nu_e}$ and $n_{\vec{k}}^{\nu_h}$, respectively, we consider only the polarization equation, [4]

$$\begin{aligned} \frac{d}{dt} p_{\vec{k}}^{\nu_e\nu_h} = & -i\omega_{\vec{k}}^{\nu_e\nu_h} p_{\vec{k}}^{\nu_e\nu_h} - i\Omega_{\vec{k}}^{\nu_e\nu_h} \left(n_{\vec{k}}^{\nu_e} + n_{\vec{k}}^{\nu_h} - 1\right) \\ & - \left(\Gamma_{\vec{k}}^{\nu_e} + \Gamma_{\vec{k}}^{\nu_h}\right) p_{\vec{k}}^{\nu_e\nu_h} + \sum_{\vec{q}} \left(\Gamma_{\vec{k}\vec{q}}^{\nu_e} + \Gamma_{\vec{k}\vec{q}}^{\nu_h}\right) p_{\vec{k}+\vec{q}}^{\nu_e\nu_h} \ . \end{aligned} \tag{7}$$

In Eq. (7), the transition frequency $\omega_{\vec{k}}^{\nu_e\nu_h}$ and the Rabi frequency $\Omega_{\vec{k}}^{\nu_e\nu_h}$ contain modifications (exchange shift and Coulomb field renormalization, respectively) due to many-body interactions. Carrier-carrier correlations, when treated at the level of quantum kinetic theory in the Markovian limit, give the terms in the second line. These terms describe screening (imaginary part) and dephasing (real part), and consist of diagonal ($p_{\vec{k}}^{\nu_e\nu_h}$ term) and nondiagonal

($p^{\nu_e \nu_h}_{\vec{k}+\vec{q}}$ term) contributions. To account for deviation from ideal two-dimensional quantum confinement because of finite quantum-well thickness and confinement potential, we modify the Coulomb potential energy with a form factor involving integrals of the envelope part of the quantum-well eigenfunctions. The numerical solution of (7) requires as input the electron and hole dispersions and the dipole matrix elements. We calculate these quantities using $\vec{k} \cdot \vec{p}$ theory and the envelope approximation for the wurtzite crystal symmetry. [12] The effects of the screening of the quantum-confined Stark effect is taken into account by the iterative solution of the $\vec{k} \cdot \vec{p}$ Hamiltonian and Poisson equation. [13] Input parameters to the bandstructure calculations are the bulk material parameters. Table 1 of Ref. [13] gives the values for the alloy $In_{0.2}Ga_{0.8}N$ considered in this paper.

The carrier density N at each location in the gain region is determined by the steady state solution of the carrier density rate equation [11]

$$\frac{\partial N}{\partial t} = 0 = \frac{J(y)}{ed} - \gamma_{eff} N - \frac{G(N)}{2\hbar\omega} \left(|v_+|^2 + |v_-|^2 \right) , \tag{8}$$

where $J(y)$ is the injection current density, d is the sum of the quantum well widths, and γ_{eff} is an effective rate for carrier loss from spontaneous emission and nonradiative processes. The carrier density $N(y, z, t)$ in Eq. (8) is averaged over the transverse variation, i.e.,

$$N(y, z, t) = \frac{1}{d} \int_{-\infty}^{\infty} dx \; N(x, y, z, t) \; . \tag{9}$$

So, the laser simulation involves the simultaneous solution of Eqs. (3) and (8), which are coupled via the gain G and the carrier-induced refractive index δn_g in Eqs. (4) and (5), respectively. In terms of the numerics, a complication is the determination of the diffusion contributions as represented by the second order derivatives in Eq. (3). The numerical evaluation of these derivatives is accomplished using the Crank-Nicholson method [14].

III. Gain and Carrier-induced refractive index

Earlier studies involving near-infrared semiconductor lasers have shown the importance of the semiconductor gain medium on optical beam quality. [3] In this section, we use Eqs.

(4) to (7) to study the gain and carrier-induced refractive properties for the nitride material system under different experimental conditions. The results are used in later sections to determine the lateral mode dependence on laser configuration.

One important difference between nitride and conventional near-infrared semiconductor gain media is the presence of the quantum-confined Stark effect in the former. To illustrate its role, we consider $Ga_{0.2}In_{0.8}N/GaN$ quantum-well structures of well widths 2 nm and 4 nm. Figures 1 and 2 show the gain G and the product $K_0\delta n_g$ as functions of photon energy for different carrier densities. As reported earlier [15], the noticeable differences in the spectra may be traced to the differences in the strength of the quantum-confined Stark effect for the two quantum well widths. For the narrow 2 nm quantum well, strong quantum confinement limits modifications to the bound state energies and dipole matrix elements by the piezoelectric or spontaneous polarization fields. As a result, both gain and phase shift spectra shown in Fig. 1 exhibit carrier density dependences that are basically similar to those of conventional near-infrared III-V laser structures, where the quantum-confined Stark effect is absent. In contrast, the weaker quantum confinement in the wide 4 nm quantum well results in greater modifications of band structure properties by the piezoelectric or spontaneous polarization fields. These fields can cause an appreciable separation between the confined electron and hole eigenfunctions, significantly reducing the optical dipole matrix element. A high carrier density ($N > 10^{13} cm^{-2}$) is then necessary to screen the fields and produce gain. Because of the higher carrier densities, the gain spectra for the 4 nm quantum well shown in Fig. 2 (a) are broader than the ones showing similar peak gains in the 2 nm case. The gain spectra also exhibit the effects of the blue shift in the band gap energy with increasing carrier density due to screening of the quantum-confined Stark effect. Also affected by the quantum-confined Stark effect is the carrier density dependence of δn_g. As in the 2 nm quantum well, δn_g for the 4 nm quantum well has a bandfilling contribution, which decreases δn_g with increasing carrier density. However, there is also a strong contribution from the gradual screening of the quantum-confined Stark effect with increasing carrier density, which increases the dipole matrix element. Because δn_g is proportional to the

square of the dipole matrix element, this contribution counters that due to band filling. Both contributions approximately cancel each other, resulting in a weak carrier density dependence, as depicted in Figure 2 (b).

The antiguiding factor [3]

$$R = -2K_0 \left(\frac{\partial \delta n_g}{\partial N}\right) \left(\frac{\partial G}{\partial N}\right)^{-1} , \tag{10}$$

gives a useful measure of the tendency for filamentation in a gain medium. Figure 3 depicts the peak gain G_{pk} dependence of R at the gain peak, where a laser typically operates. For the 2 nm quantum well and a threshold gain of around 1000 cm^{-1}, R is greater than 6, which is almost a factor of three higher than typical in near-infrared quantum-well lasers. A large antiguiding factor means a greater likelihood for filamentation. One contribution to the high R is the higher joined density of states because of the significantly heavier electron and hole effective masses in nitride compounds. For the 3nm and 4 nm quantum wells, R is smaller. The reason for the lower antiguiding factor at low peak gain, is the contributions from the screened quantum-confine Stark effect on δn_g, as discussed earlier.

IV. Filamentation

Figure 4 illustrates the formation of a filament when injection current is increased. The lateral field distributions are computed for different excitations, and a gain-guided laser operating with a 2 nm $In_{0.2}Ga_{0.8}N/GaN$ quantum well gain region. We have written the lateral field distribution in the form

$$v(y,z) = \sqrt{I(y,z)} \exp\left[-i\theta(y,z)\right] , \tag{11}$$

where $I(y,z)$ and $\theta(y,z)$ are the laser field intensity and phase averaged over the transverse dimension of the gain region. Plotted in the figure are $I(y,0)$ and $\theta(y,0)$ versus the lateral dimension y, where the plane end facets are positioned at $z = 0$ and $z = L$. We chose a resonator length $L = 500$ μm, confinement factor $\Gamma = 0.032$, facet reflectivities $R_1 = R_2 = 0.18$, and an effective internal optical loss of $\alpha_{abs} = 30cm^{-1}$. The unsaturated carrier distribution

for the 6 μm stripe width is calculated using the current spreading model by Hakki [16]. For the present calculations, we ignore the effects of well width and composition variations in the InGaN quantum well gain region. Experiments estimate cluster dimensions that are smaller than the laser wavelength. Therefore, their effects on optical propagation should be negligible. However, the inhomogeneous broadening due to well width and composition variations will change the local gain and carrier-induced refractive index seen by the laser field, and these changes may be estimated by statistically averaging over the relevant fluctuations. [17]

Near threshold, the lateral intensity distribution extends over the entire pumped region defined by a stripe width [solid curve in Fig. 4 (a)]. Antiguiding by the gain medium and diffraction give rise to a diverging wavefront as depicted by the solid curve in Fig. 4 (b). The dashed and dotted curves, for $J/J_{th} = 1.05$ and 1.10, show narrowing of the lateral intensity distribution with increasing excitation. The threshold current density J_{th} is determined by performing the wave-optical calculations with decreasing J until a vanishingly small laser field results. Along with the beam narrowing is the transition from a diverging wavefront to a converging one. This transition marks the onset of filamentation. The noticeably narrower lateral intensity lobes are commonly referred to as filaments. They occur when the intracavity intensity is sufficiently high to cause spatial hole burning. Because the carrier-induced refractive index δn_g increases with decreasing carrier density, a waveguide is formed at the spatial hole. The channeling of the laser field by the waveguide leads to the burning of a deeper hole, which in turn further concentrates the laser intensity at the spatial hole (self-focusing).

To see explicitly the narrowing of the lateral intensity distribution with increasing excitation, we plot in Fig. 5 the full width at half maximum $w_{1/2}$ of the lateral intensity distribution $I(y, 0)$ as a function of J/J_{th}. The two sets of curves for the 2 nm and 4 nm $Ga_{0.2}In_{0.8}N/GaN$ quantum-well lasers show some common behaviors. Close to threshold, while $w_{1/2}$ increases with stripe width, its dimension remains noticeably smaller than the width of the pumped region. This is especially true for the wide stripe widths (4 μm and

6 μm for the 2 nm quantum well gain region; 6 μm and 8 μm for the 4 nm quantum well region). For these stripe widths, the laser output from both gain regions undergoes a transition from a single lobe intensity distribution that occupies most of the stripe to a much narrower filament, and in some situations to multiple filaments.

Comparison of $w_{1/2}$ for the 2 nm and 4 nm quantum well gain regions illustrates the role of the quantum-confined Stark effect. The quantum-confined Stark effect, which weakens the carrier density dependence of δn_g, is stronger in the 4 nm quantum well than the 2 nm one. A result is the clearly wider lateral beam widths for the 4 nm quantum well compared to the 2 nm quantum well case. For each gain region, there is an asymptotic filament width that is independent of stripe width. This asymptotic filament width is approached at high excitation when the focusing due to the gain medium is balanced by diffraction. As shown in Fig. 5, the asymptotic filament width for the 2 nm quantum well gain region is considerably smaller than for the 4 nm quantum well gain region ($w_{1/2} \approx 2$ μm versus 4 μm). To prevent beam breakup (i.e. multiple filaments in the output beam) at high excitations, one should use a stripe width that is close to the asymptotic filament width. For the $2nm$ quantum-well active region, a single-lobe field distribution may be maintained far above threshold if the stripe width is reduced to 2 μm, which is consistent with recent experiments involving fundamental-mode operation of InGaN quantum-well lasers. [18] For the 4 nm quantum-well laser with the same resonator geometry (but with $\Gamma = 0.064$ because of the wider quantum well), a stripe width of 4 μm gives a $w_{1/2}$ that is independent of excitation. as shown in the Fig. 5.

Filamentation effects may be mitigated by reducing internal optical losses. A smaller α_{abs} allows one to reach threshold with a smaller confinement factor. A smaller confinement factor has the effect of reducing the influence of the gain medium. The result of decreasing absorption losses from $\alpha_{abs} = 30$ cm^{-1} to $\alpha_{abs} = 15$ cm^{-1} and 0 is shown in Fig. 6. The combinations of α_{abs} and Γ are chosen to maintain a constant material threshold gain of $G_{th} = 2 \times 10^3 cm^{-1}$.

V Effects of Facet Reflectivity

In this section, we describe the effects of facet reflectivity on filamentation. The end facets in nitride lasers are sometimes coated to reduce threshold current. With a smaller outcoupling loss, one can, for example, use fewer quantum wells to provide the necessary gain, thereby decreasing threshold current density. Figure 7 (a) shows the threshold current density reduction, relative to that of the uncoated device, with increasing facet reflectivity. The result is calculated under the condition that the confinement factor is decreased as the facet reflectivities are increased, so that the material threshold gain remains constant. Furthermore, we assume a 10 μm wide stripe laser operating with a 4 nm $In_{0.2}Ga_{0.8}N$ quantum well gain region.

Increasing the facet reflectivity, however, exacerbates the problem of filamentation, because it increases the recycling of a converging intracavity laser field. As discussed earlier, one consequence of filamentation is that the resulting spatial hole burning leads to multimode operation. In Fig. 7 (b), the shaded region shows the extent of single-mode operation, as predicted in our simulations. The ordinate is $\eta_{ss}^{\max} = J_{ss}^{\max}/J_{th}$, where $J_{ss}^{\max}$ is the maximum injection current for a stable steady-state solution to exist. For excitations higher than $\eta_{ss}^{\max}$, the numerical analysis does not lead to steady-state solutions, and the customary interpretation is that the laser operation is multimode. Figure 7 (b) indicates that even by balancing the increase in facet reflectivity with a corresponding decrease in confinement factor, filamentation effects dominate. The result is a reduction in the excitation range for single-mode operation with increasing facet reflectivity.

Figure 7 (b) also shows an interesting behavior around $0.5 < R_1 = R_2 < 0.6$, where two regions of single-mode operation are separated by a region where steady-state solutions do not exist. The cause for this behavior is a change in lateral mode when going from one single-mode region to the other. Specifically, for $0.5 < R_1 = R_2 < 0.6$, the laser mode switches from an output with a flat phase front to one that is tilted (beam steering). In other cases, the modal switch may be from a single lobe lateral intensity distribution to

a double lobe one. For certain ranges of facet reflectivities, the transition is mediated by an excitation range where there are no stable steady-state solutions. The range of facet reflectivities where this anomaly occurs depends on the stripe width.

From an application standpoint, changes in the output beam phase distribution, such as those just discussed, are undesirable. Quite a number of the resonator configurations in Fig. 7 have strong dependence of the lateral phase distribution on excitation. An example is shown in Fig. 8, where we see significant tilt and focus introduced to the lateral phase front with relatively small changes in excitation. Because these aberrations are not constant, their removal is not possible using conventional optics.

VI Unstable Resonators

In this section, we explore the use of unstable resonators to improve modal properties. Figure 9 shows the two possible unstable resonator configurations: positive branch unstable resonator and negative branch unstable resonator. [7] As depicted in the figure, these resonators are characterized by diverging wavefronts, which we hope will counter the focusing effects of filamentation. While unstable resonators, when used in conventional near-infrared semiconductor lasers, have led to high single-mode power [19], there are concerns regarding their ability to counter the stronger filamentation tendency in a nitride gain medium.

Figure 10 addresses some of those concerns. Plotted are the lateral field distributions at the output facet of an unstable resonator InGaN laser, and at different excitations. The optical resonator is a negative-branch unstable resonator consisting of a plane mirror and a concave mirror of radius of curvature $\rho_2 = 400$ μm. The resonator length is 500 μm and the stripe width is 10 μm. To enhance the effects of the curved facet, we use high mirror reflectivities, $R_1 = R_2 = 0.8$. Furthermore, to minimize self-focusing effects of the gain region, we chose a 4 nm $In_{0.2}Ga_{0.8}N/GaN$ quantum well gain region (refer to Fig. 3 and related discussion). A confinement factor of $\Gamma = 0.034$ is used, which gives a material threshold gain, $G_{th} = 10^3 cm^{-1}$. Figure 10 (a) shows uniform intensity distributions that overlap well with the broad gain region. Changes in the phase distribution with excitation,

a problem with high reflectivity mirrors (as shown in Fig. 8), are practically negligible [see Fig. 10 (b)]. The numerical simulations show an output power that scales linearly with injection current density, and little change in the lateral mode shape for excitations beyond twice the lasing threshold. The contribution of the concave mirror becomes evident when one notes that according to Fig. 7, a laser with $R_1 = R_2 = 0.8$ and plane facets operates multimode for $J/Jth > 1.5$.

Figure 11 compares the unstable resonator field distribution with that of the plane-plane resonator with uncoated facets. While both lasers operate single-mode at twice the threshold current, the laser with the plane-plane resonator has a sharply peaked intensity distribution that can lead to material damage. Both lasers have relatively smooth phase distributions, so imaging optics should be relatively uncomplicated. Figure 12 depicts the far-field intensity distributions for the lasers. We note that the intensity variations in the unstable resonator near-field do not result in noticeable degradation of the far field. In the calculations of the far fields, we have removed the aberrations due to tilt and defocus, as they are easily correctable with conventional optics.

We also learned from a parametric study that the laser field distributions are relatively insensitive to concave mirror radius of curvature for the range 200 μm $\leq \rho_2 <$ 500 μm. For $\rho_2 <$ 200 μm, the high magnification results in high lasing thresholds. Note that the resonator becomes stable for radius of curvature $\rho_2 >$ 500 μm. In the stable resonator configuration, single-mode operation is predicted for $J/Jth \leq 2$ and 500 μm $< \rho_2 <$ 4000 μm. However, the stable resonator modes have narrow lateral widths that are considerably smaller than the 10 μm wide gain region.

Because filamentation effects can be significantly stronger in nitride lasers than in conventional near-infrared semiconductor lasers, the range of workable unstable resonators is more restrictive. For example, the curved facet must be highly reflective. The same negative branch unstable resonator as in Fig. 10, but with uncoated facets, has narrow and sharply peaked field distributions that are very similar to those of the plane-plane resonator. We also find that the positive branch unstable resonator is not as effective in countering filamenta-

tion effects. Wide lateral intensity distributions that overlap reasonably well with the 10 μm wide gain region are obtained only with convex mirror curvature, $\rho_2 < 200\mu$m. The small radius of curvature leads to high laser threshold currents. In addition, the resulting laser output is highly diverging, with most of the intensity concentrated in two off-axis peaks. Finally, we are unable obtain single-mode performance comparable to that described in Fig. 10, for the 2nm wide quantum well structure, because filamentation effects are significantly stronger than in the 4nm quantum well case.

VII Conclusion

In summary, a wave-optical model that is coupled to a microscopic gain theory is used to investigate lateral mode behavior in group-III nitride quantum well lasers. Beam filamentation due to self-focusing in the gain medium is found to limit a fundamental-mode output to narrow stripe lasers or to operation close to lasing threshold. Filamentation effects are generally stronger in a nitride quantum well gain medium than in that of a conventional near-infrared semiconductor laser, because of heavier electron and hole effective masses. In addition, there is a strong quantum-well width dependence because of the quantum-confined Stark effect. Increasing mirror reflectivities in plane-plane resonators, which is the typical approach to reducing lasing threshold current, exacerbates the filamentation problem. However, the intracavity beam spreading effects of an appropriately designed unstable resonator can balance the focusing effects of the gain medium, resulting in fundamental-mode operation in broad-area InGaN quantum well lasers at high excitations. For nitride lasers, negative-branch unstable resonators are preferable to the more commonly used positive-branch unstable resonators, in terms of sensitivity to mirror curvatures and reflectivities, as well as in terms of obtaining fundamental modes with broad and relatively uniform intensity distributions.

This work was supported in part by the U. S. Department of Energy under contract No. DE-AC04-94AL85000.

Sandia is a multiprogram laboratory operated by Sandia Corporation, a Lockheed Martin Company, for the United States Department of Energy under contract DE-AC04-94AL85000.

References

[1] S. Nakamura and G. Fasol, *The Blue Laser Diode* (Springer, Berlin, 1997).

[2] I. Akasaki and H. Amano, 'Crystal growth and conductivity control of group III nitride semiconductors and their application to short wavelength light emitters,' Jpn. J. Appl. Phys., vol. 36 pp. 5393-5408, 1997.

[3] P. Kirkby, A. Goodwin, G. Thompson and P. Selway, 'Observation of self-focusing in stripe geometry semiconductor lasers and the development of a comprehensive model of their operation.' IEEE J. Quantum Electron., vol. QE-13, pp. 705-719, 1977.

[4] W. W. Chow and S. W. Koch, *Semiconductor-Laser Fundamentals: Physics of the Gain Materials* (Springer, Berlin, 1999).

[5] J. S. Im, H. Kollmer, J. Off, A. Sohmer, F. Scholz and A. Hangleiter, 'Reduction of oscillator strength due to piezoelectric fields in $GaN/Al_xGa_{1-x}N$ quantum wells,' Phys. Rev. B, vol. 57, pp. R9435-R9438, 1998.

[6] H. S. Kim, J. Y. Lin, H. X. Jiang, W. W. Chow, A. Botchkarev and H. Morkoc, 'Piezoelectric effects on the optical properties of $GaN/Al_xGa_{1-x}N$ multiple quantum wells,' Appl. Phys. Lett., vol. 73, pp. 3426-3428, 1998.

[7] A. E. Siegman, *Lasers* (University Science Books, Mill Valley, 1986).

[8] A. P. Bogatove, P. G. Eliseev, M. A. Man'ko, G. T. Mikaelyan and Y. M. Popov, 'Injection laser with an unstable resonator,' Sov. J. Quantum Electron. **10**, 620 (1980).

[9] R. R. Craig, L. W. Casperson, O. M. Stafsudd, J. J. J. Yang, G. Evans and R. Davidheiser, 'Etched-mirror unstable-resonator semiconductor lasers,' Electron. Lett., vol. 21, pp. 62-63,

1985.

[10] J. Salzman, T. Venkatesan, R. Lang, M. Mittelstein and A. Yariv, 'Unstable resonator cavity semiconductor lasers,' Appl. Phys. Lett., vol. **46**, pp. 218-220, 1985.

[11] W. W. Chow, S. W. Koch and M. Sargent III, *Semiconductor-Laser Physics* (Springer Verlag, Berlin, 1994), Chap. 10.

[12] S. L. Chuang and C. S. Chang, 'k·p method for strained wurtzite semiconductors,' Phys. Rev. B, vol. 54, pp. 2491-2504, 1996.

[13] W. Chow, M. Kira and S. W. Koch, 'Microscopic theory of optical nonlinearities and spontaneous emission lifetime in group-III nitride quantum wells,' Phys. Rev. B, vol. 60, pp. 1947-1952, 1999.

[14] J. Crank and P. Nicholson, 'A practical method for numerical evaluayions of solutions of partial differential equations of the heat conduction type,' Proc. Cambridge Phil. Soc., vol. 43, pp. 50-66, 1947.

[15] W. W. Chow, H. Amano and I. Akasaki, 'Theoretical analysis of filamentation and fundamental-mode operation in InGaN quantum well lasers,' Appl. Phys. Lett., vol. 75, pp. 1647-1649, 2000.

[16] B. Hakki, 'Carrier and gain spatial profiles in stripe geometry lasers,' J. Appl. Phys., vol. 44, pp. 3021-3028, 1973.

[17] W. W. Chow, A.F. Wright, A. Girndt, F. Jahnke and S. W. Koch, 'Microscopic theory of gain for an InGaN/AlGaN quantum well laser,' Appl. Phys. Lett., vol. 71, pp. 2608-2610, 1997.

[18] S. Nakamura, M. Senoh, S Nagahama, T. Matsushita and T. Mukai, 'High-power InGaN-based violet laser diodes with a fundamental transverse mode,' Extended Abstracts of the 1999 International Conference on Solid State Devices and Materials, Tokyo, pp. 224-225, Sept. 21-24, 1999.

[19] M. Tilton, G. Dente, A. H. Paxton, J. Cser, R. K. DeFreez, C. E. Moeller and D. Depatie, 'High power, nearly diffraction-limited output from a semiconductor laser with an unstable resonator,' IEEE J. Quantum Electron., vol. QE-27, pp. 2098-2108 1991.

Figure Captions

Fig. 1. Room temperature (a) gain and (b) product of wavevector and carrier-induced refractive index spectra for 2 nm $In_{0.2}Ga_{0.8}N/GaN$ quantum-well structures. The carrier densities are $N = 4.4 \times 10^{12} cm^{-2}$ (solid curve), $4.6 \times 10^{12} cm^{-2}$ (dashed curve) and $4.8 \times 10^{12} cm^{-2}$ (dotted curve)

Fig. 2. Room temperature (a) amplitude gain and (b) product of wavevector and carrier-induced refractive index spectra for 4 nm $In_{0.2}Ga_{0.8}N/GaN$ quantum-well structures. The carrier densities are $N = 2.2 \times 10^{13} cm^{-2}$ (solid curve), $2.4 \times 10^{13} cm^{-2}$ (dashed curve) and $2.6 \times 10^{13} cm^{-2}$ (dotted curve).

Fig. 3. Antiguiding factor at the gain peak for 2 nm, 3nm and 4 nm $In_{0.2}Ga_{0.8}N/GaN$ quantum-well structures vs. peak gain.

Fig. 4. Lateral (a) intensity and (b) phase distributions at output facet for $6\mu m$ stripe width laser with $2nm$ $In_{0.2}Ga_{0.8}N/GaN$ quantum well gain region. The excitation levels are $J/J_{th} = 1.01$ (solid curve), 1.05 (dashed curve) and 1.10 (dotted curve).

Fig. 5. Full width at half maximum $w_{1/2}$ of the lateral intensity distribution vs. excitation for different stripe widths. The quantum well structures are 2 nm $In_{0.2}Ga_{0.8}N/GaN$ quantum well structure and 4 nm $In_{0.2}Ga_{0.8}N/GaN$ quantum well structure.

Fig. 6. Full width at half maximum $w_{1/2}$ of the lateral intensity distribution vs excitation for a 2 nm $In_{0.2}Ga_{0.8}N/GaN$ quantum well gain region and stripe width $w = 6$ μm. The curves are for $\alpha_{abs} = 30$ cm^{-1} and $\Gamma = 0.032$ (solid curve), $\alpha_{abs} = 15$ cm^{-1} and $\Gamma = 0.025$ (dashed curve), and $\alpha_{abs} = 0$ cm^{-1} and $\Gamma = 0.017$ (dotted curve).

Fig. 7. (a) Threshold current density (normalized to that of the uncoated device) vs. facet reflectivity for a 4 nm $In_{0.2}Ga_{0.8}N/GaN$ quantum well gain region and stripe width $w = 10$ μm. (b) Maximum relative excitation for single-mode operation vs facet reflectivity for same devices as in (a).

Fig. 8. Lateral (a) intensity and (b) phase distributions at output facet for $10\mu m$ stripe

width laser with 4 nm $In_{0.2}Ga_{0.8}N/GaN$ quantum well gain region and facet reflectivities $R_1 = R_2 = 0.5$. The excitation levels are $J/J_{th} = 1.45$ (solid curve), 1.55 (dashed curve) and 1.65 (dotted curve).

Fig. 9. Positive and negative branch unstable resonators.

Fig. 10. Lateral (a) intensity and (b) phase distributions at output facet for $10\mu m$ stripe width laser with 4 nm $In_{0.2}Ga_{0.8}N/GaN$ quantum well gain region and unstable resonator with plane and $R_{2c} = 400$ μm concave mirrors. The excitation levels are $J/J_{th} = 1.05$ (solid curve), 1.50 (dashed curve) and 1.90 (dotted curve).

Fig. 11. Lateral (a) intensity and (b) phase distributions at output facet for $10\mu m$ stripe width laser with 4 nm $In_{0.2}Ga_{0.8}N/GaN$ quantum well gain region and unstable resonator used in Fig. 10 (solid curves) and plane uncoated mirrors (dashed curves). The excitation level is $J/J_{th} = 1.90$.

Fig. 12. Lateral far-field intensity distributions for the two near field distributions shown in Fig. 11.

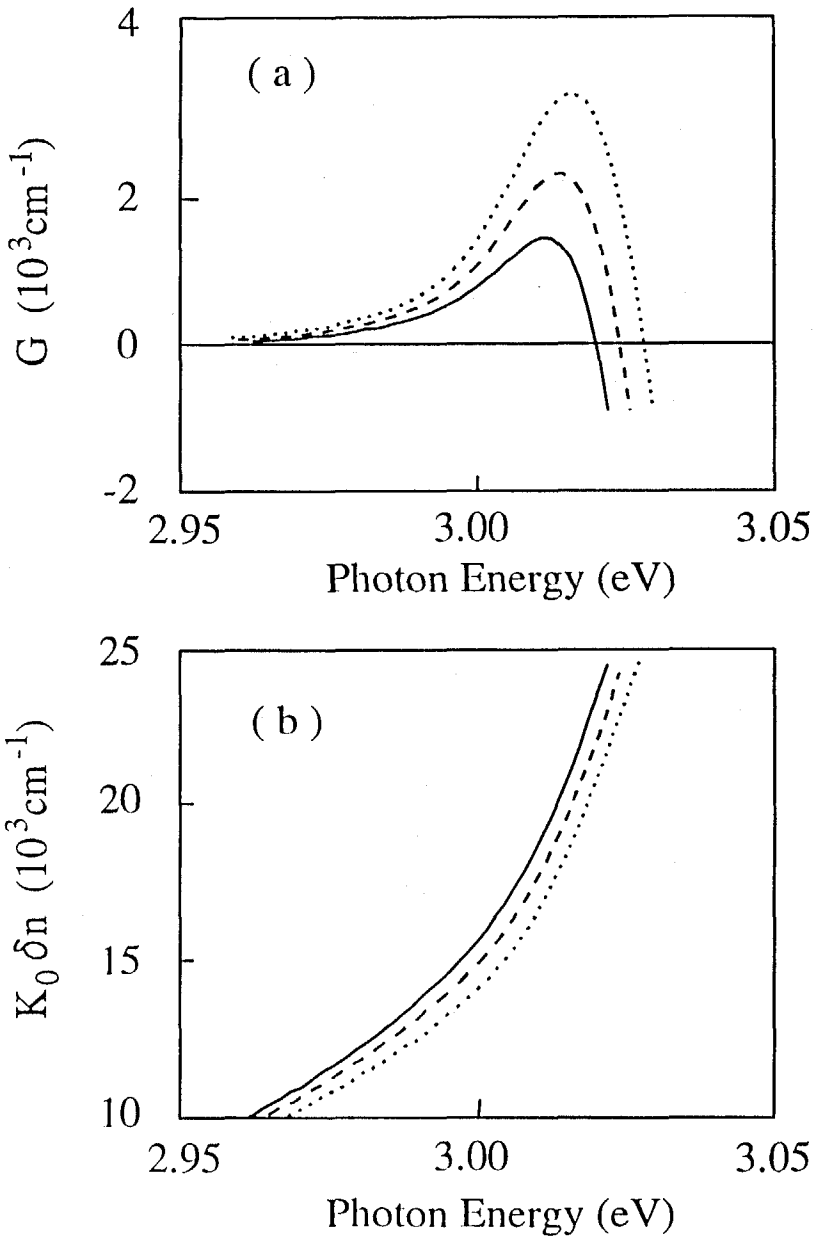
(a)
4
2
0
-2
G (10^3cm^{-1})
2.95
3.00
3.05
Photon Energy (eV)
(b)
25
20
15
10
$K_0\delta n$ (10^3cm^{-1})
2.95
3.00
3.05
Photon Energy (eV)

Chow, Fig. 1

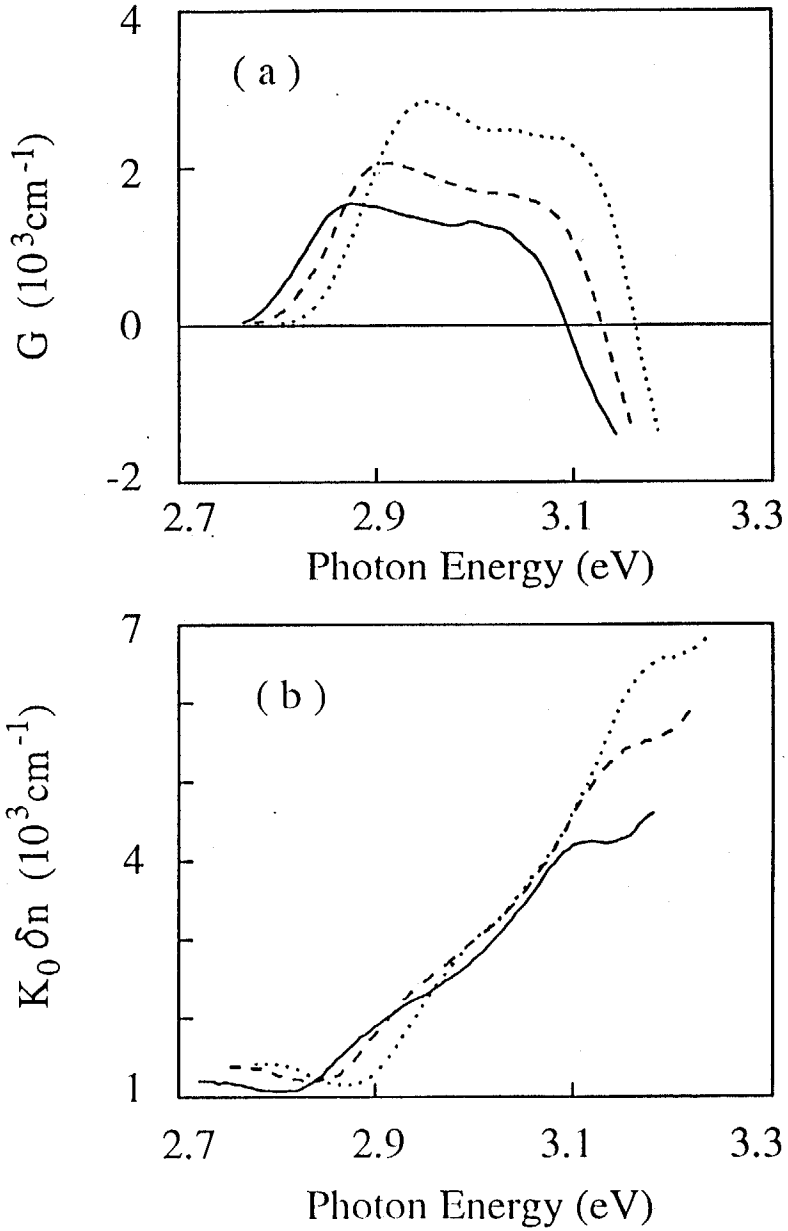
4
2
0
-2
(a)
G (10^3cm^{-1})
2.7
2.9
3.1
3.3
Photon Energy (eV)
7
4
1
(b)
$K_0\delta n$ (10^3cm^{-1})
2.7
2.9
3.1
3.3
Photon Energy (eV)

Chow, Fig. 2

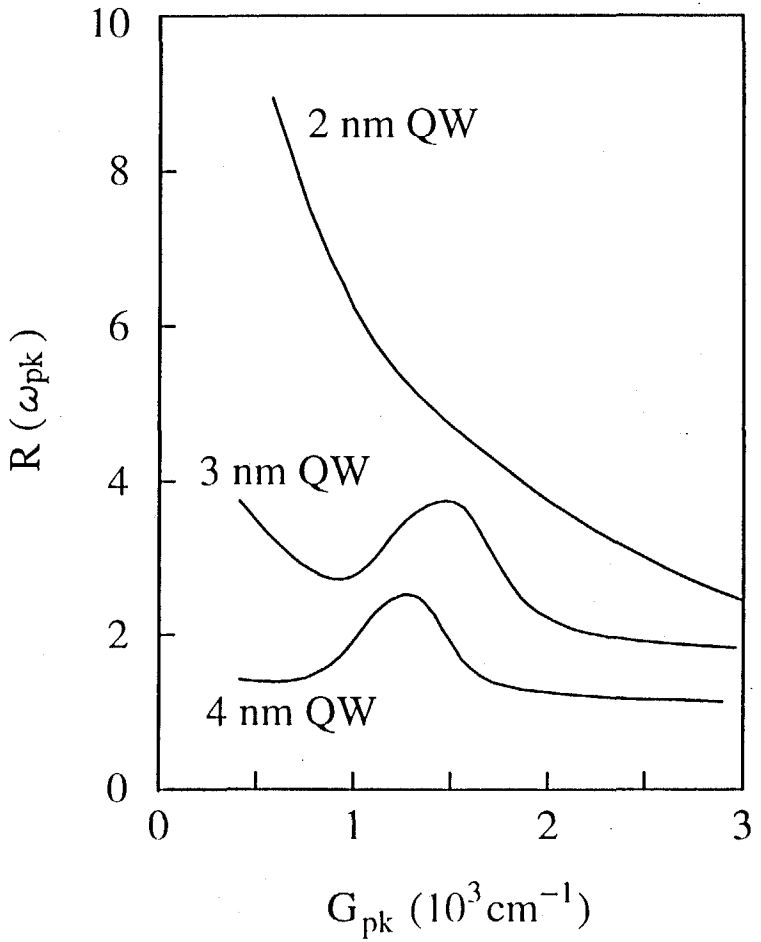

Chow, Fig. 3

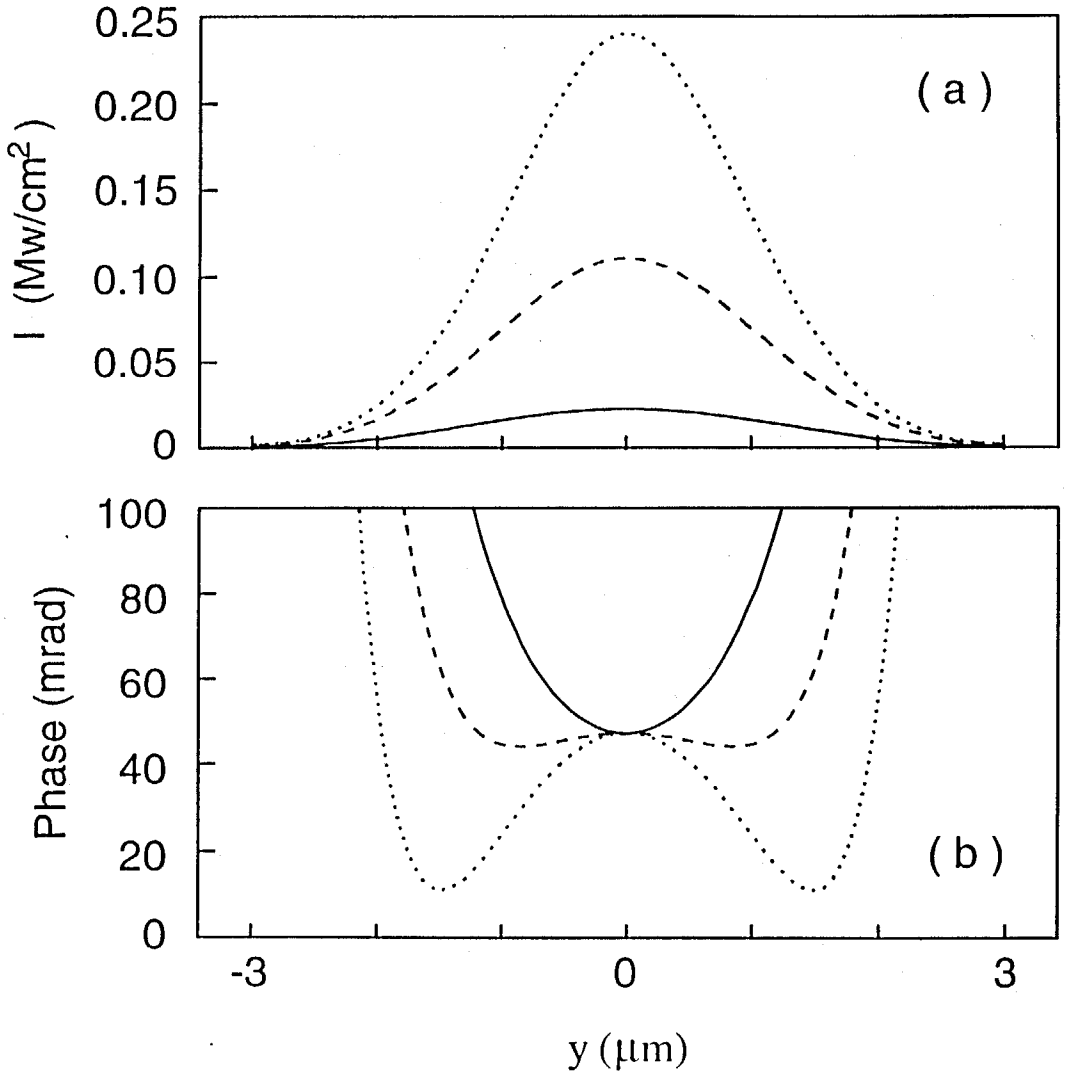
0.25
0.20
0.15
0.10
0.05
0
I (Mw/cm2)
(a)
100
80
60
40
20
0
Phase (mrad)
(b)
-3
0
3
y (μm)

Chow, Fig.4

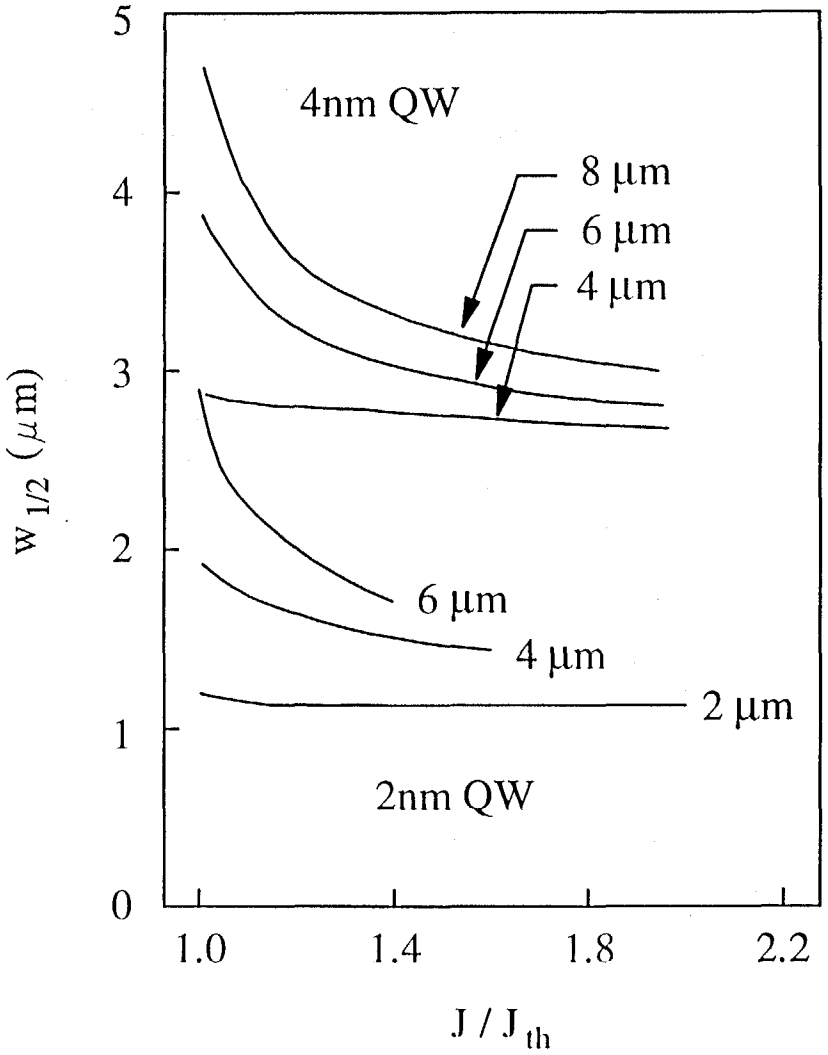
5
4
3
2
1
0
4nm QW
8 μm
6 μm
4 μm
6 μm
4 μm
2 μm
2nm QW
1.0
1.4
1.8
2.2
J / J th
w 1/2 (μm)

Chow, Fig. 5

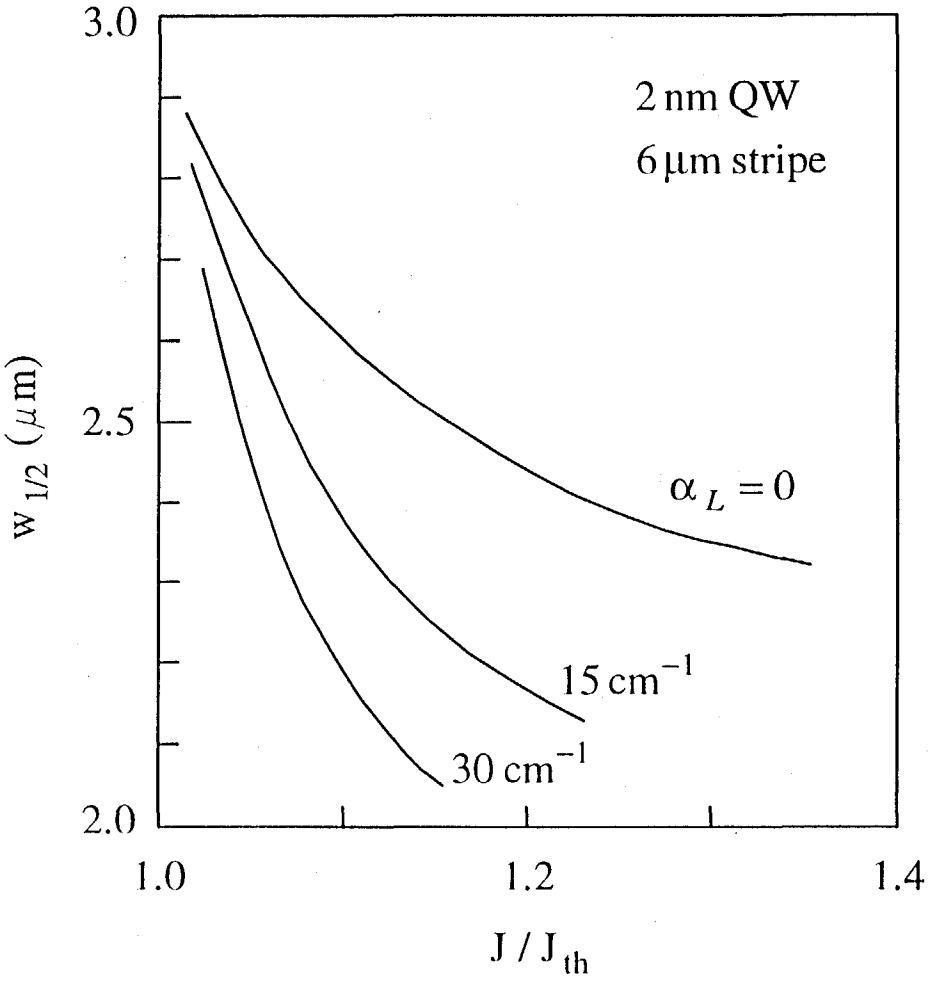
3.0
2.5
2.0
1.0
1.2
1.4
2 nm QW
6 μm stripe
$\alpha_L = 0$
15 cm^{-1}
30 cm^{-1}
$w_{1/2}$ (μm)
J / J$_{th}$

Chow, Fig. 6

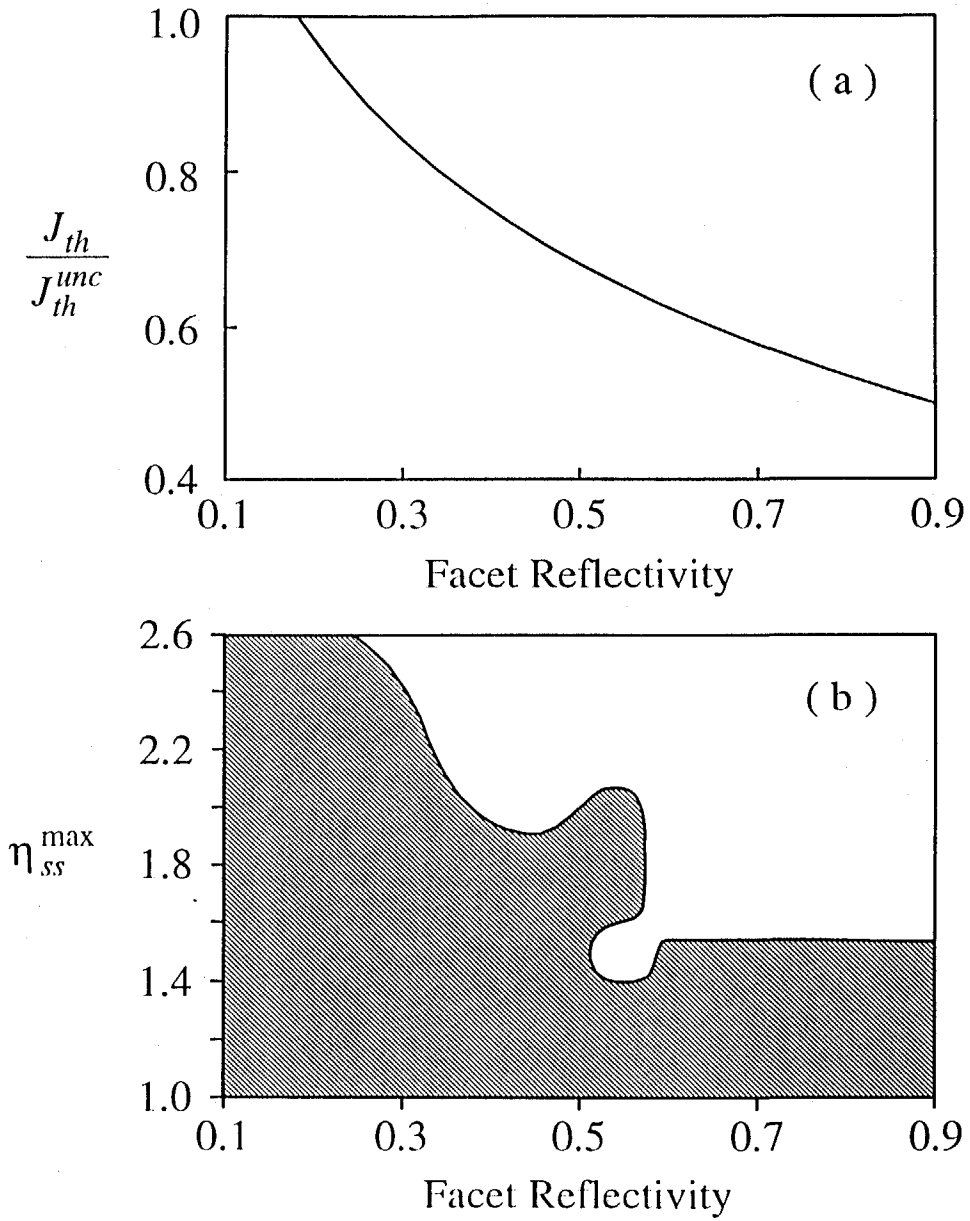
1.0
0.8
0.6
0.4
$\frac{J_{th}}{J_{th}^{unc}}$
(a)
0.1
0.3
0.5
0.7
0.9
Facet Reflectivity
2.6
2.2
1.8
1.4
1.0
η_{ss}^{max}
(b)
0.1
0.3
0.5
0.7
0.9
Facet Reflectivity

Chow, Fig. 7

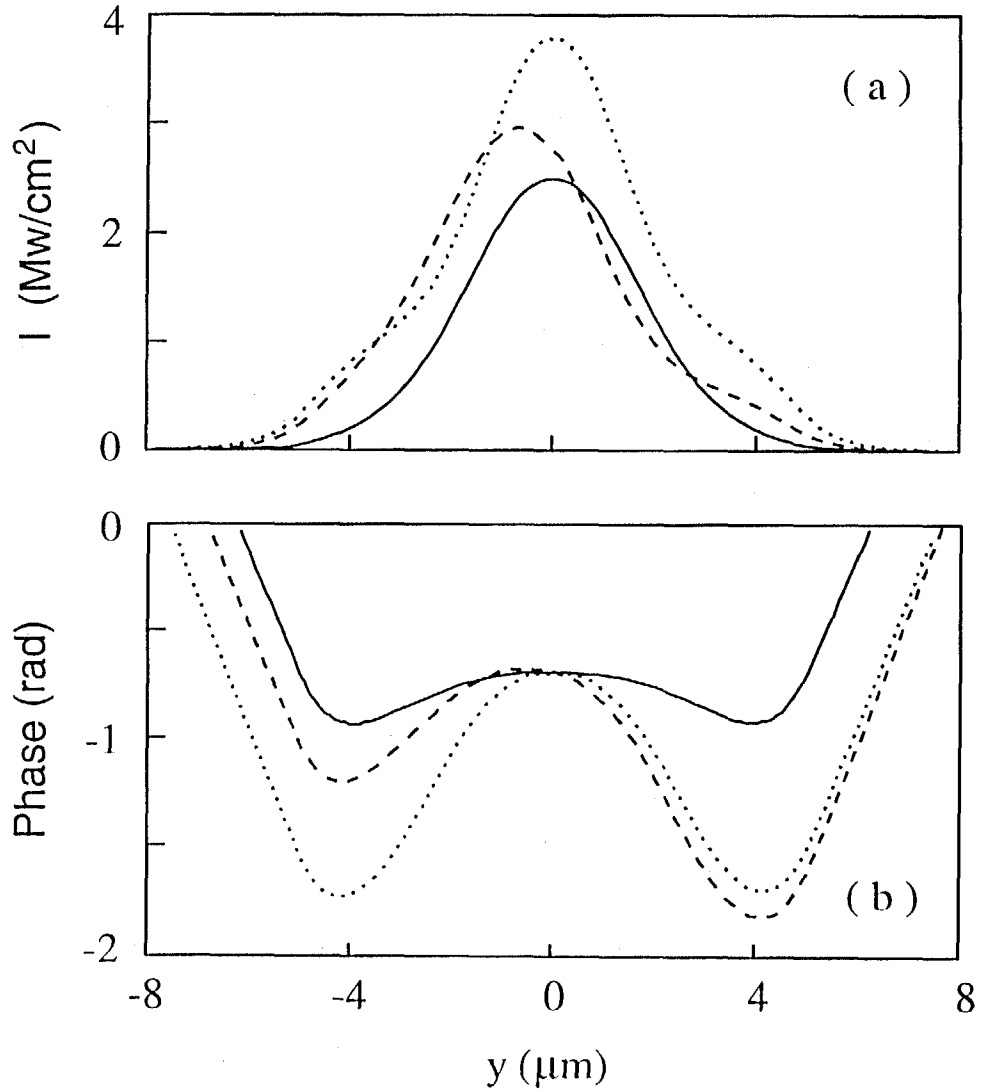

Chow, Fig. 8

positive branch

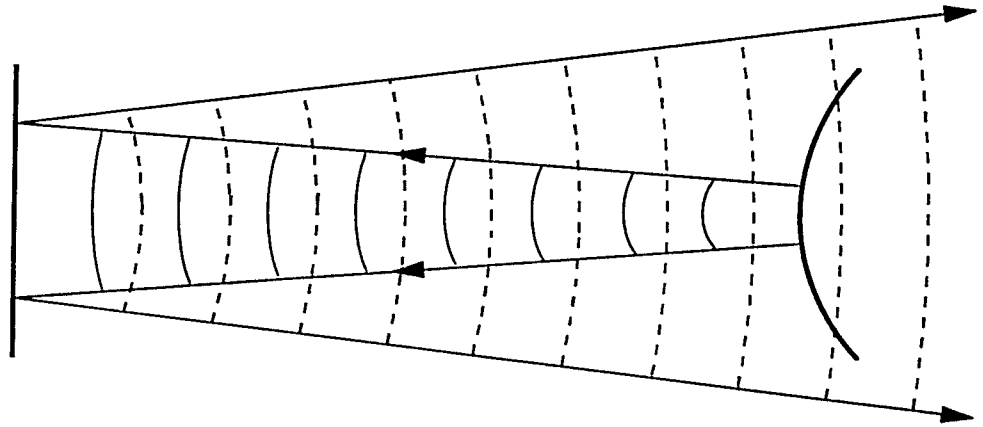

negative branch

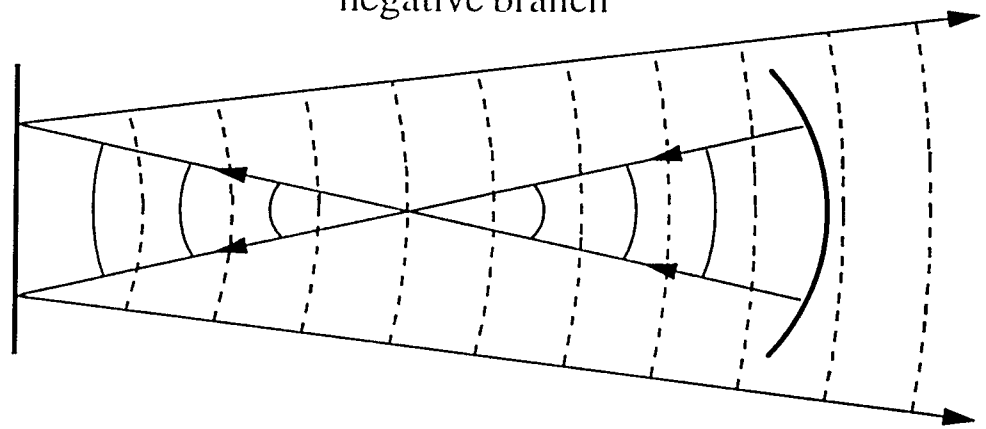

Chow, Fig. 9

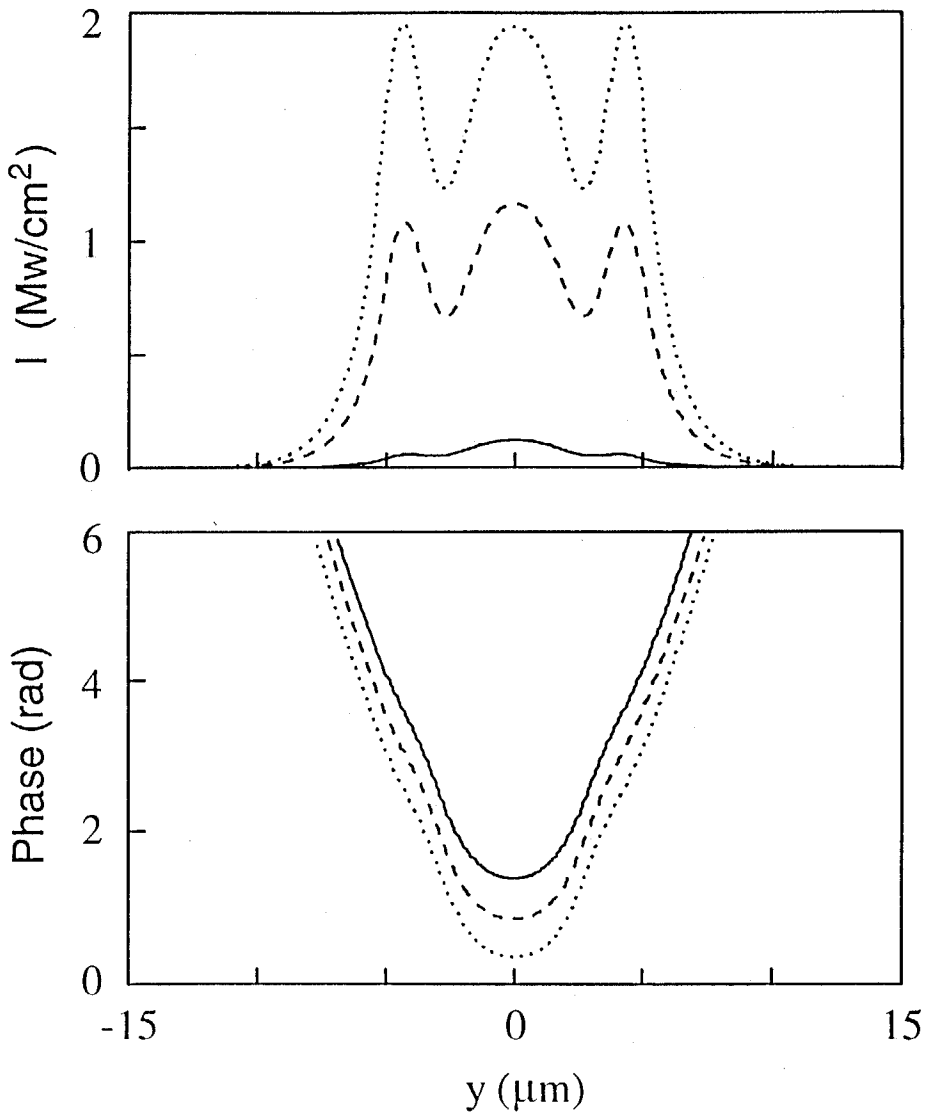

Chow, Fig. 10

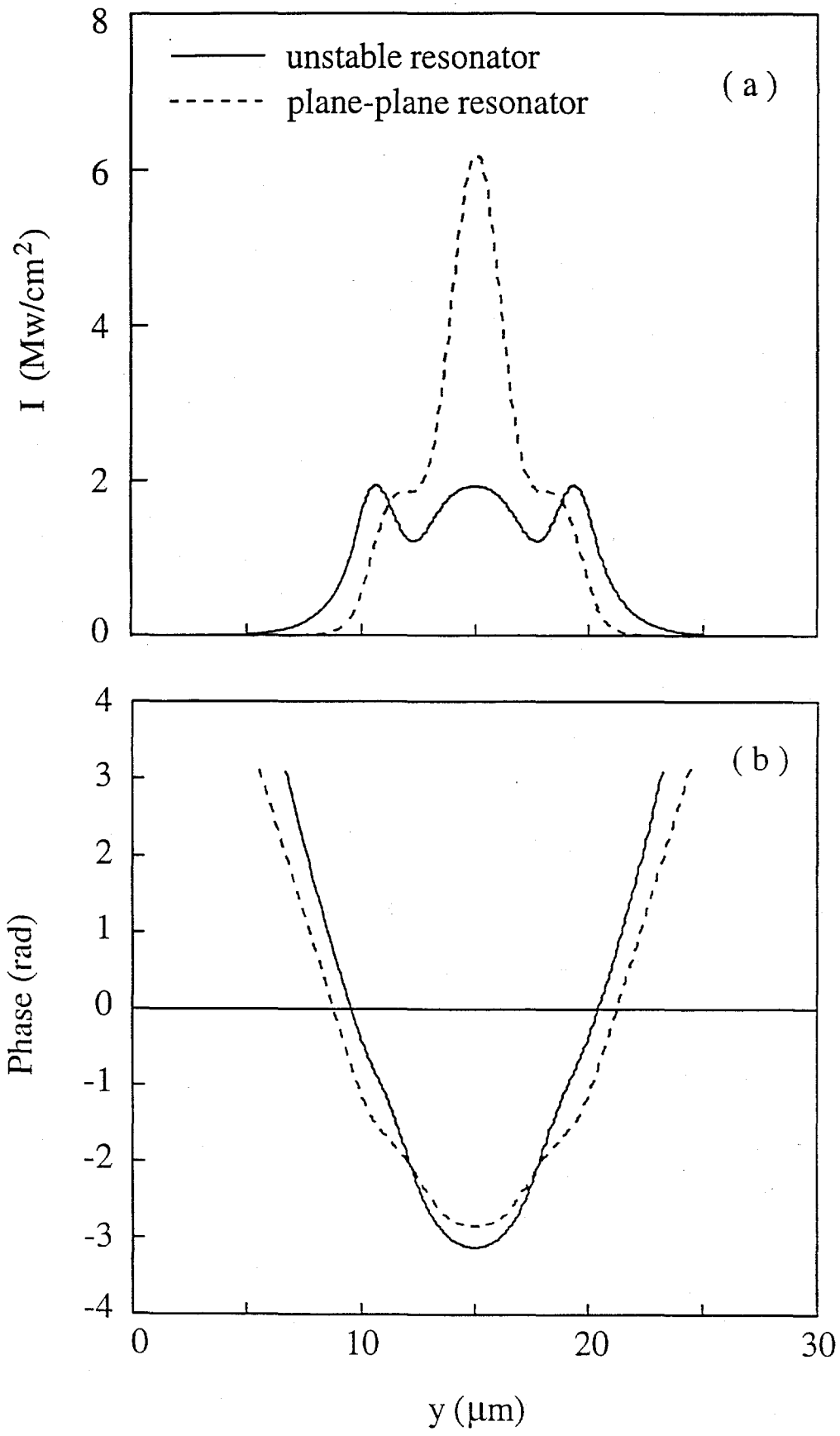
unstable resonator
plane-plane resonator
(a)
I (Mw/cm^2)
8
6
4
2
0
(b)
Phase (rad)
4
3
2
1
0
-1
-2
-3
-4
0
10
20
30
y (μm)

Chow, Fig. 11

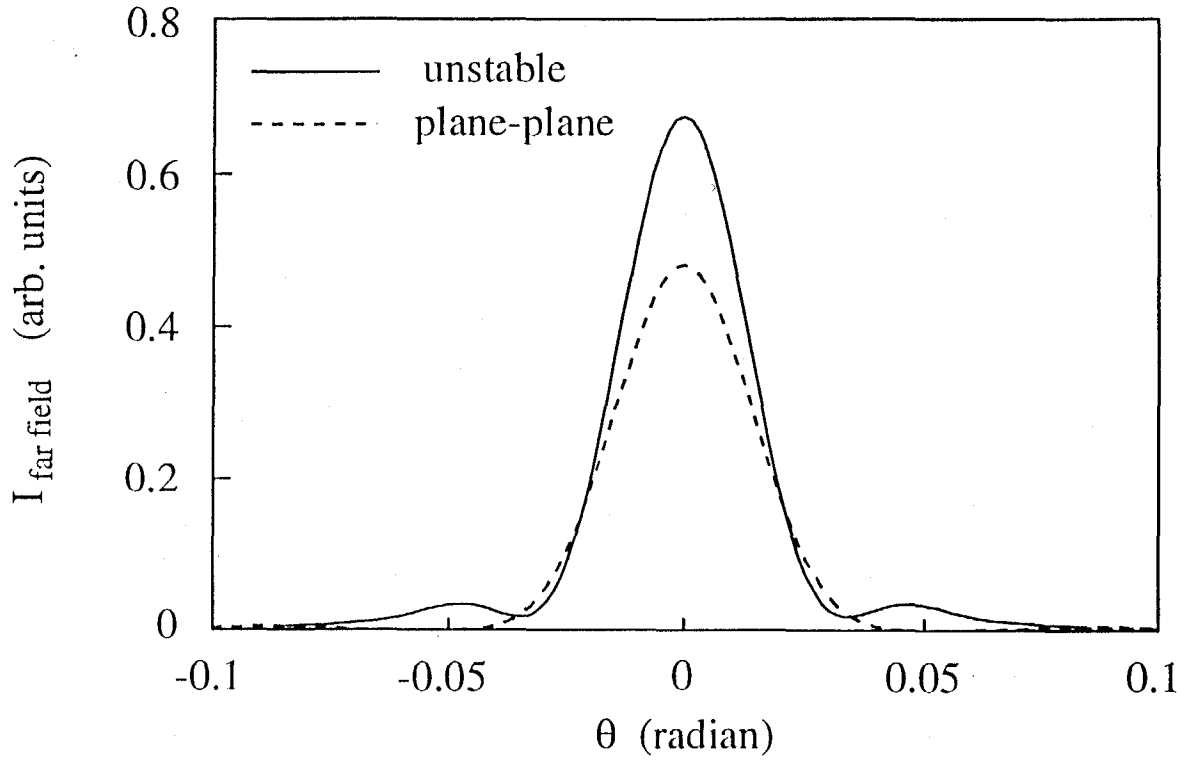
0.8
0.6
0.4
0.2
0
unstable
plane-plane
I far field (arb. units)
-0.1
-0.05
0
0.05
0.1
θ (radian)

Chow, Fig. 12